

Published in final edited form as:

Nature. 2020 March ; 579(7799): 375–378. doi:10.1038/s41586-020-2082-6.

Observations of grain boundary phase transformations in an elemental metal

Thorsten Meiners¹, Timofey Frolov², Robert E. Rudd², Gerhard Dehm¹, Christian H. Liebscher¹

¹Max-Planck-Institut für Eisenforschung, Düsseldorf, NRW, Germany

²Lawrence Livermore National Laboratory, Livermore, CA, USA

Abstract

While the theory of grain boundary (GB) structure has a long history¹ and the proposition that grain boundaries can undergo phase transformations was made already 50 years ago^{2,3}, the search for these GB transitions has been in vain. The underlying assumption was that multiple stable and metastable states exist for different grain boundary orientations^{4,5,6}. The terminology complexion was recently proposed to distinguish between those interfacial states that differ in any equilibrium thermodynamic property⁷. Different types of complexions and transitions between them have been characterized mostly in binary or multicomponent systems^{8,9,10,11,12,13,14,15,16,17,18,19}. Novel simulation schemes have provided a new perspective on the phase behavior of interfaces and showed that grain boundary transitions can occur in a multitude of material systems^{20,21,22,23,24}. However, their direct experimental observation and transformation kinetics in an elemental metal remained elusive.

Here, we show atomic scale grain boundary phase coexistence and transformations at symmetric and asymmetric [11-1] tilt grain boundaries in elemental copper (Cu). We found the coexistence of two different grain boundary structures at Σ 19b grain boundaries by atomic resolution imaging. Evolutionary grain boundary structure search and clustering analysis^{21,25,26} finds the same structures and predicts the properties of these GB phases. Furthermore, finite temperature molecular dynamics simulations explore their coexistence and transformation kinetics. Our results

Users may view, print, copy, and download text and data-mine the content in such documents, for the purposes of academic research, subject always to the full Conditions of use:http://www.nature.com/authors/editorial_policies/license.html#terms

Correspondence and requests for materials should be addressed to CHL or GD; **Correspondence and requests for simulations** should be addressed to TF.

Data availability

Datasets generated during and/or analyzed during the current study are available in Edmond – the Open Access Data Repository of the Max Planck Society, XX. All other datasets are available from the corresponding authors on reasonable request.

Author contributions

GD and CHL supervised the project. TM characterized the samples, performed all microscopy measurements and conducted the STEM image simulations. TM, GD and CHL analyzed the experimental and simulated microscopy data. TF performed GB structure search, data analysis, MD simulations and the thermodynamic analysis. TF, TM and CHL analyzed the simulated GB data. TM, CHL, TF, RER and GD wrote the manuscript.

Competing interests

The authors declare no competing interests.

Reprints and permissions information is available at www.nature.com/reprints.

demonstrate how grain boundary phases can be kinetically trapped enabling atomic scale room temperature observations.

Our work paves the way for atomic scale *in situ* studies of grain boundary phase transformations in metallic grain boundaries. In the past, only indirect measurements have indicated the existence of interfacial transitions^{9,15,27,28,29}. Now, their atomic scale role on the influence of abnormal grain growth, non-Arrhenius type diffusion or liquid metal embrittlement can be explored.

Atomic resolution observations

In this study, we focus on $\Sigma 19b$ [11-1] tilt boundaries obtained by thin film deposition of Cu on (0001) oriented Sapphire substrate (see Method section and Extended Data Fig. 1). Fig. 1 shows two variants of grain boundary phase transitions imaged at atomic resolution. The phase transition illustrated in Fig. 1a and b occurs at a near symmetric grain boundary, the one shown in Fig. 1c in a vicinal boundary. Since the grains remain the same across the structure change, the grain boundary has the same misorientation. The two structures are two phases of the same grain boundary. In both cases, two sets of characteristic structural units, referred to as pearl (blue) and domino (red) structures, are coexisting. The near symmetric boundary (Fig. 1a) has a measured misorientation angle of $\sim 48^\circ$ and the grain boundary plane inclination deviates $\sim 1^\circ$ from the perfect symmetric orientation. A ~ 11 nm long domino structure (red) segment is embedded between two pearl segments (pearl) and it is seen that the grain boundary follows a slight curvature leading to local deviations of the grain boundary plane orientation of $\sim 5^\circ$. However, facet formation is not observed. The magnified view of the right transition is shown in Fig. 1b. The domino structure is composed of double-square units alternating between low and high inclinations, as also shown in Fig. 1d. The structural unit of the pearl segment is characterized by an alternation of a curved and square-type segments (see also Fig. 1e). Both structures are separated by a grain boundary phase junction, i.e., a line defect whose line direction is perpendicular to the image plane.

The same GB phase transition is observed for a vicinal [11-1] tilt GB with an inclinational deviation of $\sim 5^\circ$ as shown in Fig. 1c. The structural units of the domino and pearl structures are nearly identical to the symmetric boundary of Fig. 1a and their detailed atomic arrangement is highlighted in Fig. 1d and e. A closer inspection of the domino structure of Fig. 1d reveals that the double-square units show a similar alignment and sequence as the symmetric boundary of Fig. 1a and b. In both cases, the regular order of the domino units is interrupted by irregular or disordered regions. The sequence of base structural units of the pearl structure, curved and square segments, is interrupted by curvy or linear subunits as shown in Fig. 1b and e. The observations reveal that two grain boundary motifs coexist at a symmetric and an asymmetric grain boundary without change in grain boundary plane orientation, misorientation and composition, carrying all the ingredients of a congruent grain boundary phase transition.

Grain boundary structure search

To investigate the structure and properties of the domino and pearl GB phases and model the structural transformations revealed by the experiment, we performed GB structure search

using atomistic calculations. The 0K grain boundary structure search was performed using evolutionary algorithm based on the USPEX code^{21,25,26}. The details of the method are described in the Method section and ref. ²¹. The results of the evolutionary search and clustering analysis of $\Sigma 19b$ (178) [11-1] GBs are illustrated in Fig. 2. The GB energy of hundreds of generated structures is plotted as a function of the number of inserted atoms [n] measured as a fraction of the bulk (178) plane parallel to the GB as shown in Fig. 2a. The lowest energy configuration predicted by our search is identified as the pearl structure, similar to that observed in the experiment. Its structure is shown in Fig. 3a and b. This ground state is located at [n] = 0, which means that the insertion or removal of atoms is not necessary. No other minima with different [n] are present, suggesting the absence of competing GB phases with higher atomic density. To identify possible metastable states, we performed clustering analysis following the methodology proposed in ref. ²¹. In this approach, the excess thermodynamic properties are used as descriptors to cluster similar GB structures and separate distinct GB phases that are expected to have different properties. Figure 2b shows the excess GB volume [V] _{n} plotted against one of the components of the excess GB stress τ_{IJ} . The plot reveals two clusters that we automatically labeled using the K-means clustering algorithms. The blue cluster contains the ground state, as seen in the inset of Fig. 2b, and corresponds to pearl-like structures, while the red cluster represents metastable GB phases relative to pearl. The examination of structures in the red cluster established that they belong to the domino phase and the inset of Fig. 2b shows the lowest energy configuration. By re-plotting the GB energy of the clustered data as a function of inserted atoms, it becomes apparent that the lowest energy configuration within the domino-like structures has the same number of atoms [n] = 0 as the pearl phase ground state, which is indicated by arrows in Fig. 2d. This analysis suggests that the structural transformation between pearl and domino GB phases is not limited by the supply of vacancies or interstitials.

Although the two GB phases have the same number of atoms with energies differing only by ~4% ($\gamma_{pearl} = 0.835 \text{ J/m}^2$, $\gamma_{domino} = 0.871 \text{ J/m}^2$), they can be clearly distinguished by other thermodynamic properties reported in Extended Table 1. The excess volumes per unit area of the lowest energy pearl and domino GB structures differ by ~36% and the grain boundary stress of the two phases is not only different, but even has an opposite sign indicating that the experimentally observed transition is of first order. The difference in the excess properties can be used to predict strains and stresses to stabilize the metastable domino phase (see Methods) as shown in Extended Data Fig. 7. At 0K, 2% lateral strain, ~5 GPa of tensile stress or 440 MPa of shear stress can stabilize the domino phase in our model.

The structural units of the lowest energy pearl and domino phases projected along the [11-1] tilt axis and viewed along [5-32] are illustrated in Fig. 3.

Simulations of GB transformations

The evolutionary search produces zero-temperature structures and we now turn to finite-temperature MD simulations to investigate the high-temperature GB behavior and GB phase transitions. Our goal here was to reproduce the experimentally observed transition between the pearl and domino GB phases and to gain new insights into the kinetics of the

transformation to explain the room-temperature stability of the two-phase states found in both the symmetric and asymmetric boundaries. We simulated pearl and domino GB structures separately at temperatures ranging from 300K to 900K using simulation blocks with periodic boundary conditions along the GB as well as blocks with boundaries terminated at an open surface (see Methods). Our simulations demonstrated that in our model system at ambient pressure the pearl structure remained the ground state at all temperatures studied. The domino structure was metastable and transformed into pearl by nucleation and growth, characteristic of first-order transitions. In agreement with the predictions of the 0K search, these simulations confirmed that the number of atoms at the GB does not change upon the transformation, i.e. the transformation is diffusionless. Figure 4a shows the simulation block after an initially uniform domino GB phase was annealed for several nanoseconds. The pearl GB phase nucleated at both open surfaces and grew inwards transforming the parent domino GB phase. The two structures are separated by a grain boundary phase junction: a line defect that separates the two structures as highlighted in Fig. 4b. The two-phase structure shown in Fig. 4c closely resembles the experimentally observed GB transition illustrated in Fig. 4d.

We also found that the velocity of the GB phase junction, which determines the rate of the transformation, strongly depends on temperature and the defect length along the periodic dimension y , the [11-1] tilt axis. At relatively high temperatures, such as 650K, a complete transformation of the GB structure (Fig. 4) can occur within few tens of nanoseconds. Further simulations (see Methods) with different sizes of the simulation block indicate that the motion of the grain boundary phase junction is length dependent, suggesting that it migrates by a kink nucleation mechanism, similar to dislocations. The nucleation barrier of this thermally activated process is apparently high enough to kinetically trap the two-phase coexisting state on the MD time scale at room temperature. When the length of the GB phase junction exceeds a few nanometers, we observe no migration of the junction at temperatures of 500K and below. These simulations suggest that the experimentally observed two-phase states do not have to be in thermodynamic equilibrium at room temperature, but are instead kinetically trapped.

To study the effect of temperature on the relative stability of domino and pearl phases we performed free energy calculations following the methodology of refs. ^{31,32}. The results of the calculations as shown in Extended Data Fig. 8 confirm that the free energy difference decreases by 30% from 0K to 800K bringing the phases closer to coexistence. We also demonstrate that equilibrium phase coexistence and reverse transformations can be observed in our model when tensile stresses of ~ 3.3 GPa or shear stresses in range of 200-350 MPa are applied at 500K (see Extended Data Fig. 9).

Our atomic-scale experimental observations of GB phase coexistence and transformations at symmetric and asymmetric tilt grain boundaries in a pure metallic system remained so far unexplored. Atomic resolution imaging uniquely reveals that the two coexisting GB phases are clearly distinct by their differing structural repeat units. In contrast to assumptions based on thermodynamic concepts⁴, GB phase coexistence is also observed at an asymmetric GB. This indicates that GB phase transitions in pure systems can also emerge at more general boundaries and thus largely influence materials properties. It is the combination of atomic-

scale observations and structure prediction that reveals that the GB phases differ in excess thermodynamic properties and that their transformation is kinetically limited.

Our GB structure search predicted both experimentally observed pearl and domino GB phases in the symmetric and asymmetric boundaries. Interestingly, the calculations showed that both GB phases have the same number of atoms, suggesting that the stability of the two-phase states seen in the experiment and simulations at room temperature cannot be explained by the need to supply atoms by diffusion. The differing excess properties of the GB phases predicted by the calculations are expected to have a strong effect on GB properties, such as diffusion, segregation or crack healing^{20,29,33}. Furthermore, the core structure and energies of disconnections of the GB phases might differ, which should affect disconnection nucleation and hence GB migration.

Our high temperature MD simulations of the GB phase transition reproduce the experimentally observed GB phases (see Fig. 1 and Fig. 4). The strong dependence of the transformation rate on temperature and the GB phase junction length suggests that the motion of GB phase junctions may require the nucleation of kink pairs and can impede the transformation at low temperatures.

The experimental observation of the coexistence of two distinct GB phases at room temperature can thus be rationalized in terms of temperature induced GB phase transformations and retarded transformation kinetics. During cooling to room temperature, the domino GB phase starts transforming into the pearl phase by nucleation. The steadily decreasing mobility of the GB phase junction eventually freezes isolated domino GB phase regions at temperatures below ~500K, making their observation possible in the experiment. Previously, a similar trapping has been only demonstrated in multicomponent, glass-forming alloys³⁴. In addition, the difference in excess properties of the domino and pearl phases suggests that stresses could potentially contribute to the stability of the domino phase. This is supported by modeling finite temperature coexistence of the GB phases at 500K under tensile stresses of ~3.3 GPa and σ_{23} shear stresses of 200-350 MPa (see Methods). While the GPa level tensile stresses are too high to be supported by the real material, the shear stresses are comparable to local shear stresses observed in previous experiments³⁵. Furthermore, it implies that in addition to temperature, shear stresses have a much stronger effect on the free energy difference than tensile stresses. Hence, we cannot rule out that stresses of few hundred MPa potentially present in the material could also influence the experimentally observed GB phase coexistence.

Conventional phase transitions in the bulk control many materials properties. Much of materials science involves the delicate interweaving of thermodynamics and kinetics, using phase transitions to sculpt advantageous microstructures. While grain boundary kinetics have long been understood to be key to attaining favorable grain structures, the possible role of grain boundary phase transitions has been neglected. They have not been studied in metals since none had been observed. The recent suggestions of modeling^{20,21,23} and now the discovery of grain boundary phase transitions in a relatively simple elemental metal opens the door to new strategies for materials design.

Methods

Cu thin films and TEM specimen preparation

The presented GB structures were obtained from Cu thin films grown by molecular beam epitaxy (MBE) on (0001) oriented Sapphire substrates at room temperature and a post deposition annealing at 673K for 3 h. The depositions were performed at the Central Scientific Facility (CSF) Materials of the Max-Planck-Institute for Intelligent Systems in Stuttgart. The global grain structure of the thin film was analyzed by electron backscatter diffraction (EBSD) in a JEOL JSM-6490 scanning electron microscope (SEM) (see also the Supplementary Information). The TEM specimens were extracted from specific locations of the thin film by an in-plane lift-out technique in a dual beam SEM / focused ion beam (FIB) instrument (Helios Nanolab 600i, Thermo Fischer Scientific).

The grain orientation, distribution of coincident site lattice (CSL) grain boundaries and the corresponding inverse pole figure of the copper thin films grown by molecular beam epitaxy (MBE) is shown in Extended Data Fig. 1. All grains have a [11-1] orientation, which is parallel to the growth direction of the thin film ideally suited for atomic structure observations at room temperature. The majority of the grain boundaries are $\Sigma 3$, $\Sigma 7$, $\Sigma 19b$ and $\Sigma 37c$ with [11-1] tilt axis highlighted in black, yellow, red and green, respectively. The grain size is $\sim 100 \mu\text{m} \pm 50 \mu\text{m}$ and shows a bimodal distribution and the grains exhibit a cylindrical shape. Residual thermal tensile stresses on the order of 100 MPa are present in the annealed Cu thin film³⁶. The shear stresses in similar thin films can show strong local variations even exceeding the average residual thermal stress³⁵. The $\Sigma 19b$ used in this study is shown in red. The white rectangle in the center of the EBSD map exemplary shows a location where a TEM specimen was extracted by focused ion beam (FIB) preparation.

Scanning transmission electron microscopy

All STEM data were acquired using a probe corrected FEI Titan Themis 60-300 (Thermo Fisher Scientific). The TEM is equipped with a high brightness field emission gun and a gun monochromator. The electrons were accelerated to 300 kV and images were recorded at a probe current of $\sim 80 \text{ pA}$ with a high-angle annular dark field (HAADF) detector (Fishione Instruments Model 3000). The collection angles for the HAADF images were set to 73-200 mrad using a semi-convergence angle of 23.8 mrad. Image series with 20-40 images and a dwell time of 1-2 μs were acquire, registered and averaged in order to minimize the effect of instrumental instabilities and noise in the images.

STEM multi-slice image simulations

STEM multi-slice simulations were performed by the Prismatic software^{37,38}. The grain boundary structures predicted by evolutionary search were used as input files for the image simulations in order to enable a direct comparison of simulation and experiment. The thickness of all simulated cells was set to 22 nm and a slice thickness of 0.2 nm was used. In total, 8 frozen phonon configurations were incoherently summed to include the thermal vibration of atoms. The pixel size was set to 10 pm. The microscope parameters, such as HAADF detector collection angles (73-200 mrad), semi-convergence angle (23.8 mrad) and primary electron energy (300 kV) were identical to the experiment.

Structure prediction by evolutionary search and clustering at 0K

Following the evolutionary approach, the algorithm samples a diverse population of different GB structures, while improving them over many generations based on the energy minimization criterion. During the search, the structures change due to heredity and mutations, atoms are inserted and removed from the GB core to identify structures with different atomic densities. The search changes the GB periodic dimensions to also sample large area reconstructions of the GB. The 0K evolutionary search was evolved over 50 generations. The search sampled different atomic densities given as the number of atoms inserted into the boundary in fraction of the (178) bulk plane ranging from 0 to 1. Four independent evolutionary searches were performed, exploring structures with number of atoms ranging from 1000 to 4500 and 100 to 600 atoms. The GB cross-section was varied during the search between the smallest possible value and a factor of 4 times. The LAMMPS code³⁹ was used to evaluate the energies of the generated structures. The GB structures were inspected and visualized with OVITO⁴⁰. Viewing perpendicular to the tilt axis along [5-32] reveals that the lattice planes in the upper crystal appear shifted for the pearl phase (Fig. 3b), but remain continuous without shift for the domino phase (Fig. 3d). The shift translation vector is inclined with respect to the image plane and is $1/6 [920]$.

The clustering analysis was performed to identify distinct grain boundary phases following the methodology proposed in refs. ^{20, 21}. The excess properties including excess volume $[V]_n$ and two components of grain boundary stress τ_{11} and τ_{22} were calculated for each generated structure. The excess volumes of the ground state pearl structure and the lowest energy domino structure are $[V]_{n,pearl} = 0.14 \text{ \AA}$ and $[V]_{n,domino} = 0.22 \text{ \AA}$, respectively. The GB excess stress of the ground state pearl structure is determined to $\tau_{11,pearl} = -1.66 \text{ J/m}^2$ and $\tau_{22,pearl} = -0.46 \text{ J/m}^2$ and for the lowest energy domino structure to $\tau_{11,domino}$ of 0.25 J/m^2 and $\tau_{22,pearl} = 0.29 \text{ J/m}^2$.

Prior to clustering, these features were scaled using the StandardScaler function implemented in the scikit-learn library. The clustering was performed using the K-means clustering algorithm also implemented in scikit-learn library.

Linking structure prediction and experimental observations

Atomic resolution observations and atomistic predictions can be directly linked by multislice STEM image simulations^{37,41}. The predicted GB structures served as input for STEM image simulations to quantitatively compare atomic peak positions and intensities at the GB core of different pearl GB structures (see Extended Data Fig. 2). For this analysis, we selected three different pearl-like structures produced by the evolutionary search including the ground state, a higher energy state with large atomic density as well as one poorly optimized configuration with high energy. The grain boundary energy of pearl structures is plotted against the number of inserted atoms $[n]$ as fraction of the (178) grain boundary plane in Extended Data Fig. 2a. The approximate locations of the input grain boundary structures used for STEM image simulations in the plot are highlighted by red, green and yellow circles, respectively. In Extended Data Fig. 2b, c and d, the corresponding projections of the GB structures along the [11-1] tilt axis and perpendicular to it are shown in the left and right panels, respectively. The ground state structure of the pearl phase, as predicted by USPEX at

0K, with a GB energy of 0.835 J/m^2 is shown in Extended Data Fig. 2b, highlighted in red. The higher energy structures with GB energies of 0.932 J/m^2 (green) and 1.023 J/m^2 (yellow) are illustrated in Extended Data Fig. 2c and d. Locations where atoms are displaced from their ideal positions with respect to the [11-1] viewing direction are marked by arrows in Extended Data Fig. 2b. The atomic displacements in these regions leads to dechannelling of the electron probe and hence a reduction of the HAADF-STEM image intensity.

An atomic resolution STEM image of the symmetric pearl structure and its structural unit are illustrated in Extended Data Fig. 3a. Visual inspection reveals an excellent agreement with the predicted ground state of the pearl phase presented in Extended Data Fig. 2a. Since the atomic column peak intensity in aberration-corrected STEM is sensitive to the number of atoms in the column, the elemental species but also atomic displacements, it can be used to quantitatively compare experiment and simulation. In Extended Data Fig. 3b to e, only the peak intensities at the grain boundary core are colored. The experimental STEM image shown in Extended Data Fig. 3b agrees best with the simulated STEM image of the ground state pearl structure illustrated in Extended Data Fig. 3c. The strong scatter in peak intensities in the simulated STEM images of Extended Data Fig. 3d and e is a result of pronounced displacements of atoms perpendicular to the [11-1] beam direction. This inhomogeneous intensity distribution originates from the higher degree of disorder at the GB core of these high energy pearl structures. The direct comparison of experiment and simulation at the atomic scale finds excellent agreement and clearly reveals that the experimentally observed pearl grain boundary structure resembles a low energy state.

Finite temperature molecular dynamics simulations

Molecular dynamics simulations were performed using the LAMMPS code³⁹ in the NVT ensemble with Nose-Hoover thermostat. To model the transition from the metastable domino phase to the pearl phase, we performed independent isothermal simulations at temperatures ranging from 300K to 900K. We used blocks with periodic boundary conditions along the boundary as well as blocks with open surfaces. The open-surface simulation methodology was introduced in ref. ²⁰ to allow for supply or outflow of atoms to the grain boundary in case it is necessary for achieving the ground state. Only periodic boundary conditions were used along the [11-1] tilt axis. We used different sizes of the simulation block to investigate the effect of the GB phase junction length on the kinetics of the transformation. The simulated GB transitions were visualized with OVITO⁴⁰. Grain boundary free energy calculations of the pearl and domino GB phases at ambient pressure were performed using harmonic and quasi-harmonic methods as described in refs. ⁴² and ^{31,32}.

To model the transition from the metastable domino phase to the pearl phase, we performed independent isothermal simulations at temperatures of 300K, 400K, 500K, 600K, 650K, 700K, 800K, 850K and 900K. We used blocks with periodic boundary conditions along the boundary as well as blocks with open surfaces. We also used different sizes of the simulation block to investigate the effect of the GB phase junction length on the kinetics of the transformation.

Symmetric tilt grain boundaries with periodic boundary conditions

We used a simulation block with dimensions $33.6 \times 34 \times 14 \text{ nm}^3$ containing 1,339,740 atoms. The z direction was normal to the GB plane. The simulations were performed for up to 200 ns. We observed a transformation of the domino phase to the pearl phase at 850K and 900K. At temperatures below 850K, the initial domino phase remained stable and well-ordered throughout the entire simulation. Based on these simulations, we estimated the limit of pearl phase stability to be around 900K. The simulations also confirmed that the supply of atoms was not necessary for the transformation.

Symmetric tilt grain boundaries with open surface

When the boundary was terminated at an open surface, we were able to observe the transition from domino to pearl at much lower temperatures. In all of these simulations the pearl phase nucleated at the surface triple junctions. The simulations showed strong effect of temperature on the kinetics of the transformation. The initial simulation block had dimensions of $45 \times 0.626 \times 14 \text{ nm}^3$ and contained 33,080 atoms. Here, the y periodic dimension, which also defines the length of the GB phase junction, was only one periodic unit length along the $[11-1]$ direction $L_y = a_0 \times 3 = 0.626 \text{ nm}$. In these quasi-2D simulations, we were able to observe the nucleation of the pearl phase at 400K, which was significantly lower compared to the homogeneous nucleation at 850K in a block with periodic boundary conditions. However, after the pearl phase nucleated, the migration of the junction was too slow and we were not able to observe a complete transformation at this temperature. At 300K we did not observe pearl phase nucleation at all. More rapid nucleation kinetics and complete transformations were observed at higher temperatures of 500K, 600K and 650K. Already at 500K, the full transformation was completed within only 13 ns of the simulation. During this time, the two GB junctions travel the distance of $L_x = 45 \text{ nm}$. In principle, these simulations allow to evaluate the velocity of the GB junction and, by approximating the driving force as the GB energy difference at 0K, even the mobility of the GB phase junction at 300K can be predicted on the experimental time-scale. However, while these simulations with the artificially short dimension $L_y = 0.626 \text{ nm}$ allowed to observe GB phase transitions at low temperatures, they are likely to overestimate the mobility of the GB phase junction.

To study the effects of the GB phase junction length, we increased the size L_y of the simulation block by replicating the initial block along the periodic direction y 40 times. The final dimensions of the simulation block were $45 \times 25 \times 14 \text{ nm}^3$ and it contained 1,323,200 atoms. The initial configurations were taken from the middle of the 500K simulation and contained both the pearl and the domino phases. We obtained the large simulation block for 200 ns at 500K and did not observe any substantial migration of the GB phase junction. This behavior was very different from a complete transformation at the same temperature in a thinner block, in which the GB phase junctions traveled the entire length L_x of 45 nm. In these simulations, we effectively froze the transformation at 500K by making the GB phase junction longer. At higher temperatures such as 650K, we observed a complete transformation again even in the thicker block during 48 ns of the simulation.

Asymmetric tilt grain boundaries

The asymmetric boundary is 6° inclined relative to the symmetric orientation. Its periodic dimensions were substantially larger than that of the symmetric boundary. As a result, we did not attempt a full grand canonical optimization of the boundary with USPEX. Instead, we used the common gamma-surface method which nevertheless generated both pearl and domino structures with energies of $\gamma_{gb} = 0.87 \text{ J/m}^2$ and 0.89 J/m^2 , respectively. Due to the different inclination, the energy difference between the two structures reduces to 1.9%, which is even smaller than that for the symmetric GB. The structures of both asymmetric pearl and domino ground states are shown in Extended Data Fig. 4. Despite the smaller energy difference at 0K, the pearl phase remains more stable at finite temperature for the asymmetric GB. MD simulations of a transformation from domino to pearl structure were performed at 600K, 700K, 800K and 900K using simulation blocks with dimensions of $34 \times 2.5 \times 3.1 \text{ nm}^3$ containing 43,248 atoms. At these temperatures, we observed complete transformations to pearl phase as illustrated in Extended Data Fig. 5a and Extended Data Fig. 5b. We intentionally used a relatively small size $L_z = 3.1 \text{ nm}$ to stabilize the asymmetric configuration. Interestingly, at a temperature of 600K, the GB in the pearl structure remained asymmetric, while at all higher temperatures the symmetric configuration appears. The nucleation of the asymmetric pearl phase from the open surfaces at 700K is shown in Extended Data Fig. 6a. The transformation from the initially asymmetric domino structure to the symmetric pearl phase is illustrated in Extended Data Fig. 6b.

Estimating stresses and strains necessary to stabilize the domino phase in atomistic simulations

Different phases of the same grain boundary (GB) can have different entropies so changing the temperature can change the relative free energies and induce a phase transformation. They can also have different excess volumes, excess stress and excess shears, so changing the stress and shear stress, respectively, can also induce transformation. Here, we use thermodynamic analysis to identify conditions under which domino and pearl GB phases can coexist in equilibrium under non-hydrostatic conditions in the model. The analysis will predict strains and stresses that could stabilize the domino phase. At equilibrium coexistence domino and pearl GB phases have the same free energies $\gamma_{domino} = \gamma_{pearl}$ ⁴³. Under general non-hydrostatic conditions the grain boundary free energy of each phase is a function of temperature, lateral strains e_{11} , e_{12} , e_{22} and stresses σ_{33} and σ_{23} as described by the Gibbs adsorption equation⁴⁴.

$$d\gamma = -[S]_N dT - [V]_N d\sigma_{33} - [B]_N d\sigma_{23} + \sum_{i,j=1,2} (f_{ij} - \delta_{ij}\gamma) de_{ij} \quad (\text{Eq. 1})$$

where $[S]_N$ is excess entropy, $[V]_N$ is excess volume, $[B]_N$ is excess shear, f_{ij} is excess grain boundary stress and γ is given by⁴⁵

$$\gamma = [U]_N - T[S]_N - \sigma_{33}[V]_N - \sigma_{23}[B]_N \quad (\text{Eq. 2})$$

just like excess volume $[V]_N$, excess shear $[B]_N$ represents extra displacement due to the boundary but in the direction of the tilt axis instead of normal to the boundary plane.

For tilt grain boundaries studied here we only consider shear stress σ_{23} which is parallel to the boundary plane and is applied in the direction of the tilt axis. Non-zero σ_{13} leads to grain boundary migration by coupled motion, breaking the thermodynamic equilibrium between the grains. As a result we restrict the equilibrium analysis to the non-hydrostatic states when σ_{13} is zero.

At 0K we calculated γ_{domino} and γ_{pearl} directly by independently varying ϵ_{11} , σ_{33} and σ_{23} following the methodology described in ref. 45. We focus on these variables because the corresponding GB excess volume, shear and stress f_{11} have the largest difference for pearl and domino phases. Extended Data Fig. 7 shows that the curves cross at about $\epsilon^*_{11} = -2\%$, $\sigma^*_{33} = 5$ GPa, and $\sigma^*_{23} = 0.44$ GPa, where the asterisk refers to coexistence conditions. These coexistence stresses and strains can also be estimated using Eqs. Eq. 1 and Eq. 2 as, $\sigma^*_{33} \approx [U]_N / [V]_N$, $\sigma^*_{23} \approx [U]_N / [B]_N$, $\epsilon^*_{11} \approx - [U]_N / (f_{11} - \gamma)$, where $[U]_N$ refers to the difference between excess energy, stress, volume and shear of pearl and domino phases at ambient conditions. For example using our 0K values $[U]_N = [U]_{N,domino} - [U]_{N,pearl} = 0.835 - 0.871 = 0.036$ J/m² and $[V]_N = [V]_{N,domino} - [V]_{N,pearl} = 0.22 - 0.14 = 0.08$ Å, we estimate the tensile stress required to stabilize domino to be $\sigma_{33} \approx 4.5$ GPa, which closely matches the direct 0K calculation shown in Extended Data Fig. Fig. 7b.

At finite temperature we can also estimate the strains and stresses required to achieve coexistence by using free energies $[U]_N - T[S]_N$ that we obtained from free energy calculations instead of just $[U]_N$. Since the free energy difference decreased with temperature according to our calculations shown in Extended Data Fig. 8, smaller stresses and strains should be required to bring the two phases to the equilibrium coexistence. For example, at 500K and zero stress the free energy difference $[U - TS]_N = [U - TS]_{N,domino} - [U - TS]_{N,pearl} = 0.028$ J/m² was obtained using harmonic approximation. Taking the excess volume difference $[V]_N = [V]_{N,domino} - [V]_{N,pearl} = 0.08$ Å we estimate the coexistence tensile stress $\sigma^*_{33} \approx 3.5$ GPa, which is smaller than the 0K value. For lateral compression, similar analysis predicts GB phase coexistence at compressive strain $\epsilon^*_{11} \approx [U - TS]_N / (f_{11} - \gamma) = 0.028$ J/m² / $(-0.621 + 2.495) = -1.5\%$. Finally, we estimate shear stress parallel to the GB plane and in the direction of the tilt axis that should stabilize the domino phase as $\sigma^*_{23} \approx [U - TS]_N / [B]_N = 0.028$ J/m² / $(0.22\text{Å} - 0.98\text{Å}) = -360$ MPa.

MD simulations of GB phase transformations and coexistence under stress

To test the predicted values of stress required to establish equilibrium coexistence between pearl and domino GB phases we perform MD simulations at 500K (see Extended Data Fig. 9). Here we focus on the coexistence due to stresses σ_{33} and σ_{23} done in two separate sets of simulations. To demonstrate equilibrium and avoid hysteresis due to nucleation, we follow the methodology commonly employed in simulations of bulk phases: we start with a simulation block containing both GB phases and then monitor the motion of the GB phase junction. At coexistence, the junction is expected to fluctuate by performing random walk, while away from the coexistence we expect to observe growth of one of the phases. The growth simulations are particularly important to rule out false coexistence due to slow kinetics of the GB junction. We used periodic boundary conditions parallel to the grain boundary plane. Along the z direction the boundary conditions were not periodic: free atoms

were sandwiched between two 20 Å thick surface layers. The boundary atoms were used to manipulate the stress state in the system. The simulation block had dimensions $100 \times 1.2 \times 14 \text{ nm}^3$ and contained 165,110 atoms.

Coexistence and transformations under tensile stress σ_{33}

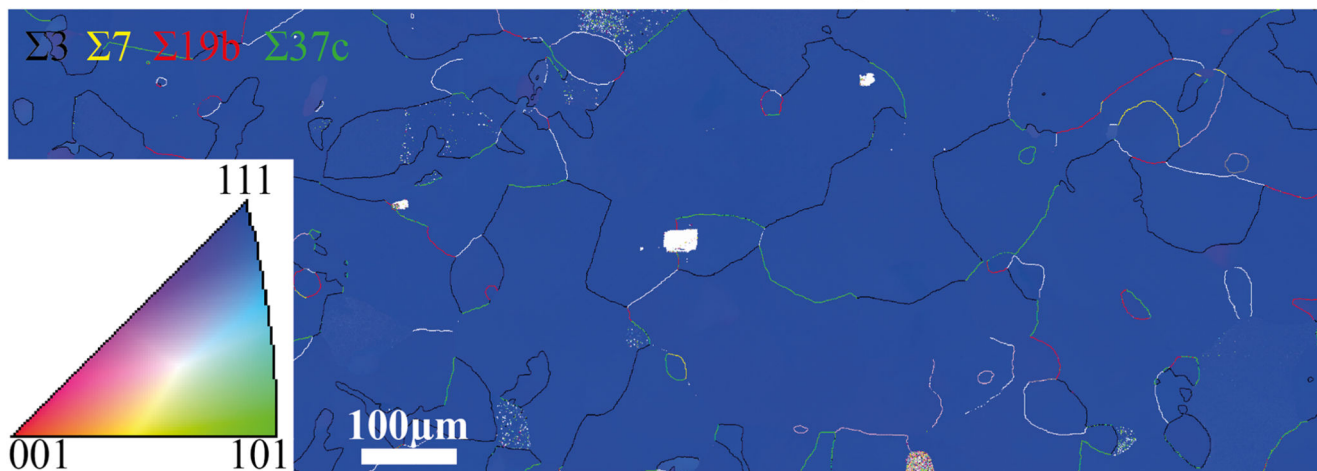
We took the initial structure with two GB phases and applied tensile strain to generate stress in the cell. We performed separate simulations with stresses $\sigma_{33} = 3.95, 3.3, 2.85$ and 0 GPa. The tensile stress was maintained by fixing the z coordinates on the 20 Å thick top boundary surface layer and fixing the bottom boundary layer of the same thickness. At the same time we allowed displacements of the atoms in the top boundary layer in the x and y directions so that the σ_{13} and σ_{23} stresses remained zero. Similar to ambient pressure simulations at $\sigma_{33} = 2.85$ GPa, we observed growth of pearl phase indicating that this tensile stress was not sufficient to stabilize the domino phase. The reverse transformation was observed at $\sigma_{33} = 3.95$ GPa. Extended Data Fig. 9c shows that domino phase grew during 400 ns at the expense of pearl phase, suggesting that this stress is above the GB phase coexistence. Finally, in the simulation at $\sigma_{33} = 3.3$ GPa we did not observe substantial growth of either of the phases indicating that this stress is close to the coexistence value. This value agrees well with prediction based on the free energy calculations and thermodynamic analysis.

Coexistence and transformations under shear stress σ_{23}

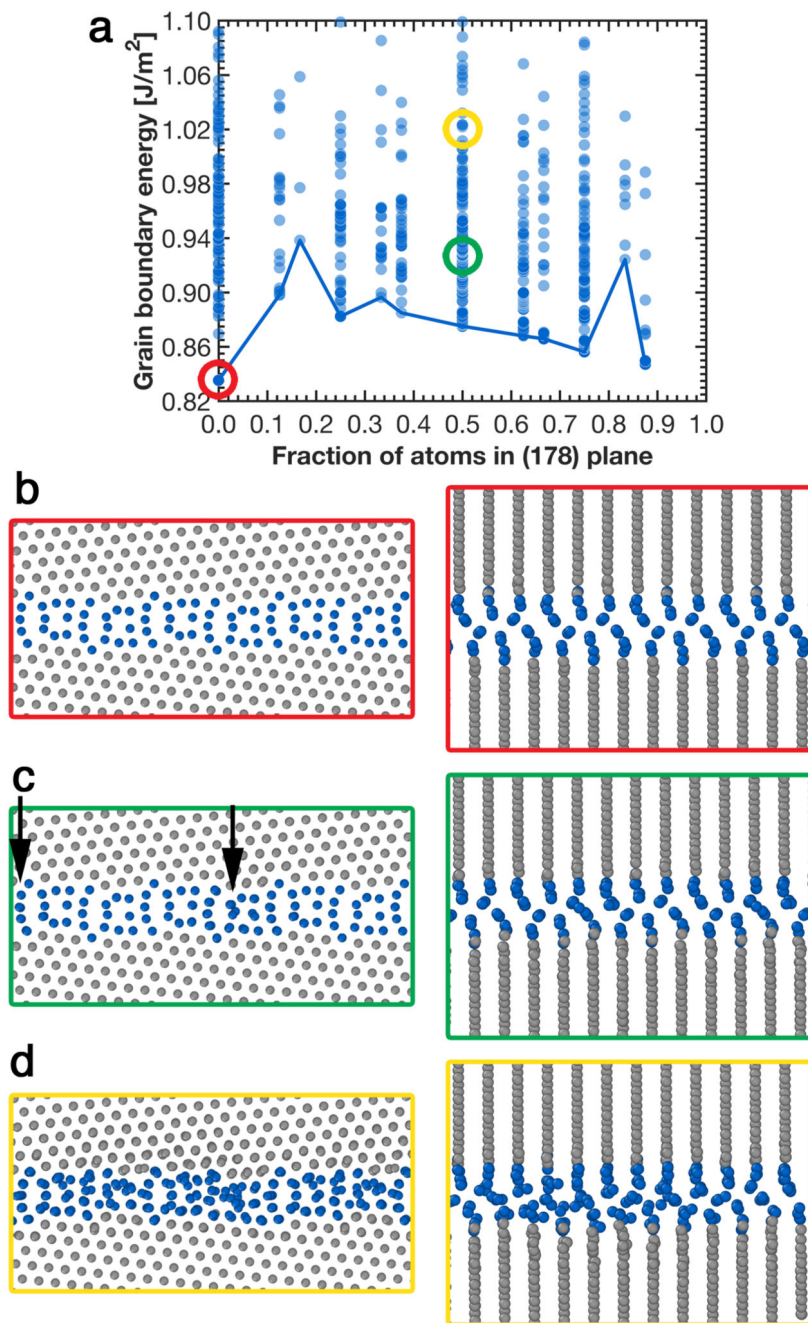
To implement the simulations under shear stress conditions, we took the same initial configuration that we used before applying the tensile stress and ran a relatively short simulation when the bottom boundary layer of atoms was fixed, while the top boundary layer of atoms was moved in small increments in the direction parallel to the tilt axis. During this simulation the shear stress increased to about 450 MPa and we saved snapshots that corresponded to different values of shear stress. The boundary atoms were allowed to move in the x and z direction so that σ_{13} and σ_{33} stresses remained zero. We then started independent simulations from different snapshots to study GB behavior under shear stresses of 200, 300, 350 and 400 MPa. Extended Data Fig. 9d shows the substantial growth of the domino phase at ~350 MPa, suggesting that this value of stress stabilizes the domino phase above the coexistence. At 200 and 300 MPa we observed very small fluctuations of the position of the GB phase junction and no apparent growth of one of the phases. Based on these observations we conclude that the coexistence shear stress is between 200-350 MPa, which is also consistent with our estimates based on the free energy calculations and thermodynamic analysis.

Extended Data

Inverse Pole Figure Map

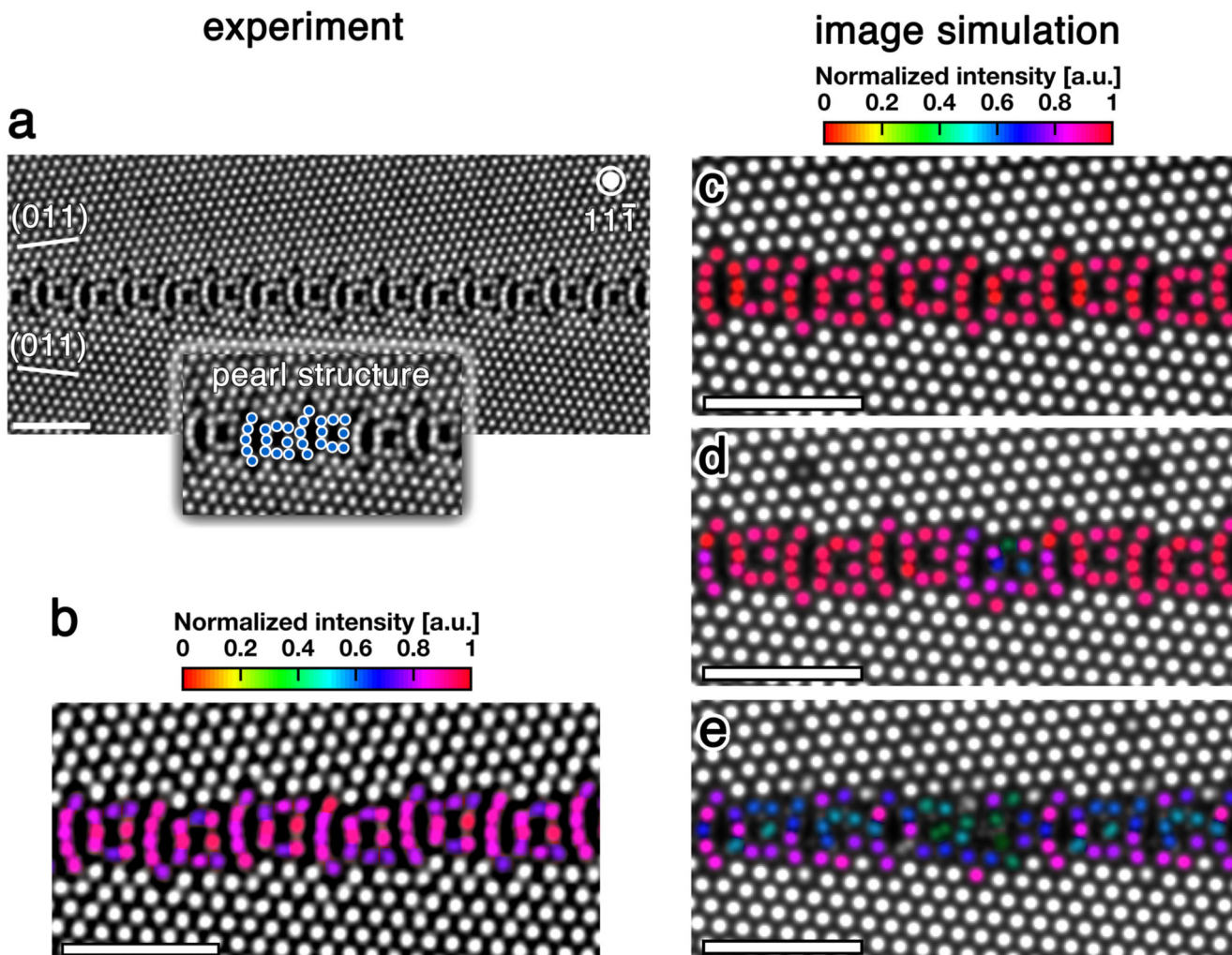
**Extended Data Fig. 1. EBSD characterization of the Cu thin film.**

The [11-1] tilt GBs have been obtained by thin film deposition of Cu on (0001) oriented Sapphire substrate. The inverse pole figure shows that all grains are in $\langle 111 \rangle$ orientation with an average grain size of 100 μm . The majority of GBs in the film are twin and low angle GBs (up to 70%), but crucially $\Sigma 7$, $\Sigma 19b$, $\Sigma 37c$ and corresponding asymmetric boundaries are also present. The most prominent GBs are colored. The $\Sigma 19b$ GBs are highlighted in red. The white rectangle in the center shows a position where a TEM specimen has been extracted.

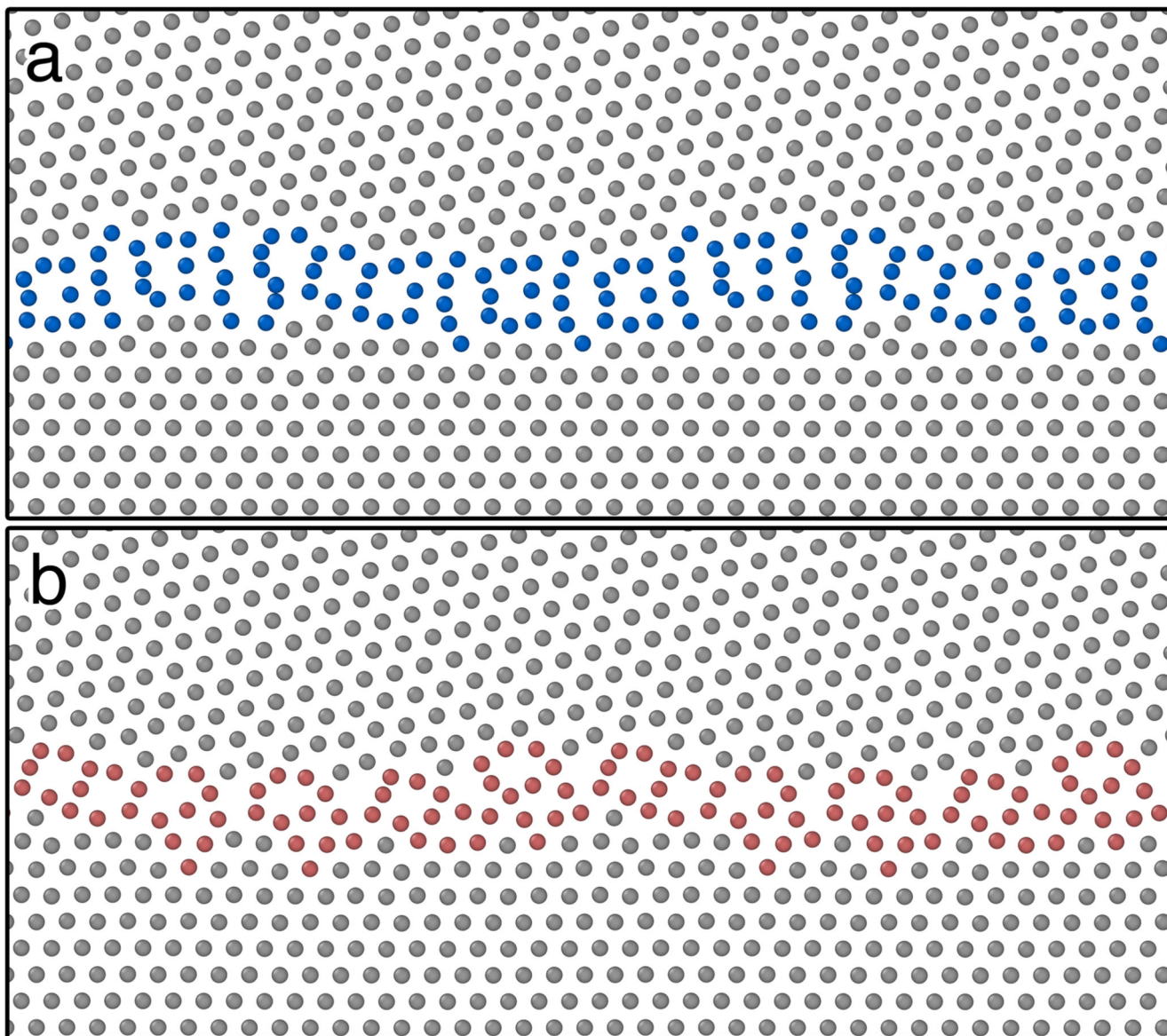


Extended Data Fig. 2. Input GB structures for STEM image simulations.

a. Grain boundary energy plotted versus the number of inserted atoms [n] as fraction of the (178) grain boundary plane. The red, green and yellow circles indicate the locations of the GB structures shown in **b** to **d**. **b** to **d** show the three GB structures used for STEM image simulation. The left panel shows the structure along the tilt axis [11-1], the right panel perpendicular to the tilt axis. The colored boxes indicate where these structures are located in the energy plot.

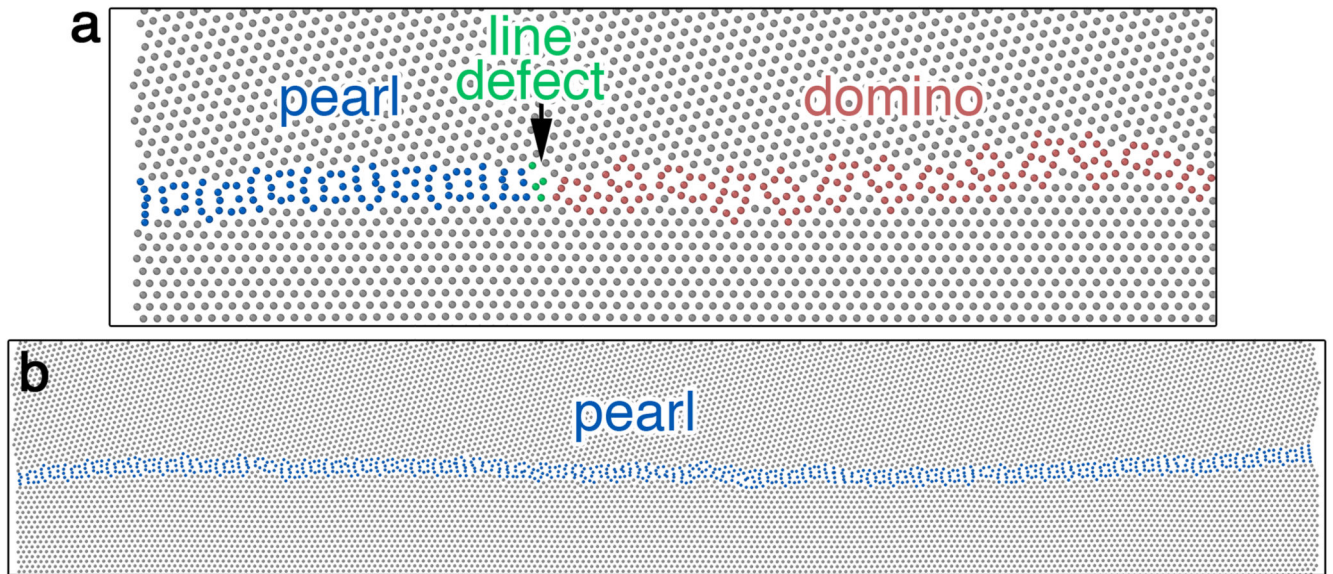


Extended Data Fig. 3. Linking atomic resolution observations and structure prediction. **a**, Aberration corrected HAADF-STEM image of the symmetric $\Sigma 19b$ (178) [11-1] pearl phase. Its structural unit is highlighted in the inset. **b**, Color coding of the experimental grain boundary structure based on atomic column peak intensities. **c-e**, Simulated STEM images of the predicted grain boundary structures by USPEX for a sample thickness of 22 nm. The same color coding as in **b** was applied. **c**, Lowest energy structure with GB energy of 0.835 J/m² and $[n] = 0$, **d**, medium energy GB with 0.932 J/m² and **e**, high energy GB with 1.023 J/m², both with $[n] = 0.5$. The scale bar is 1 nm in all images.



Extended Data Fig. 4. Asymmetric grain boundary structures.

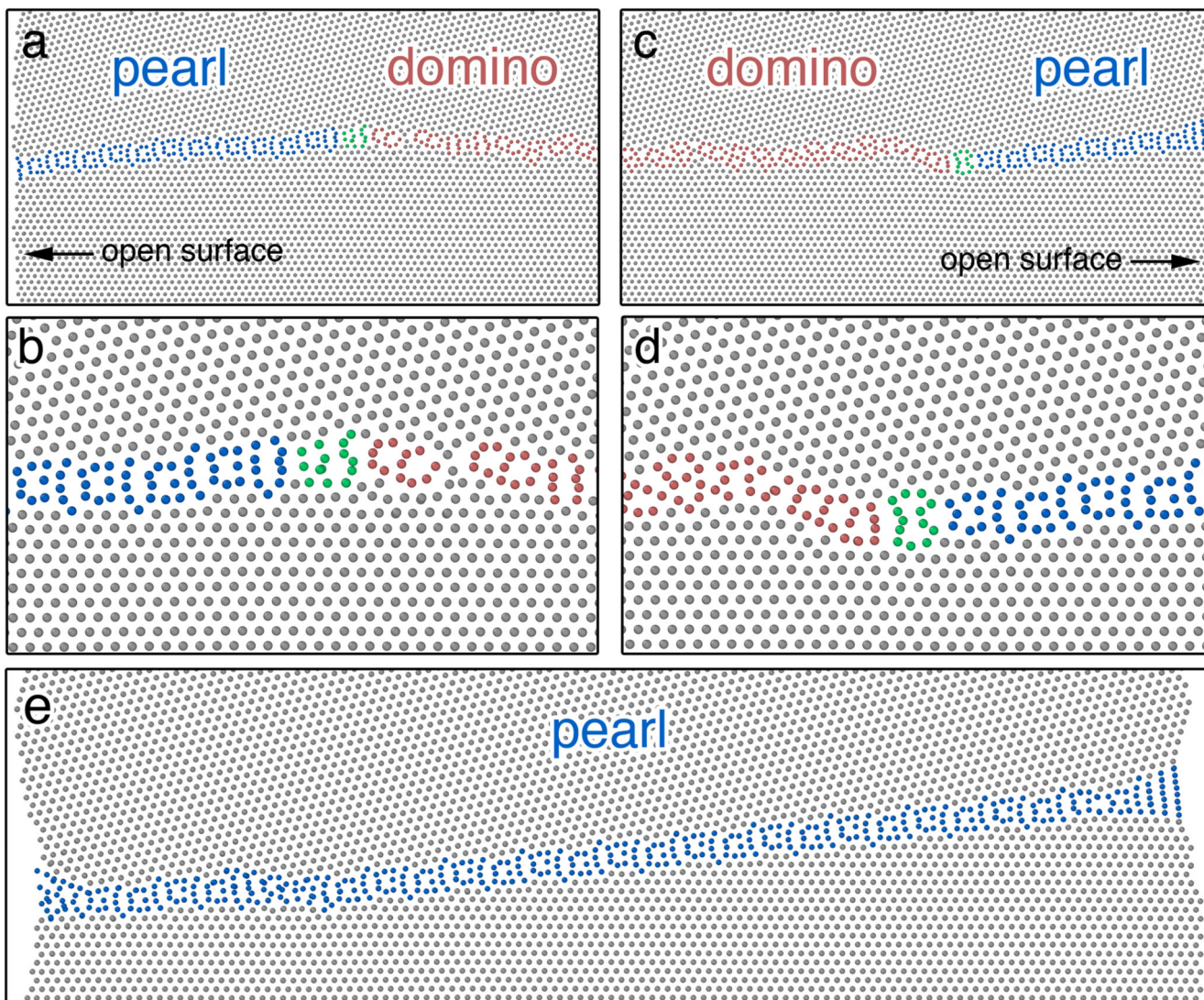
a, Ground state pearl and **b**, metastable domino structures of the asymmetric boundary at 0K. The two structures have the same number of atoms and correspond to two different translations of the bulk grains relative to each other.



Extended Data Fig. 5. Asymmetric grain boundary transformation at 600K.

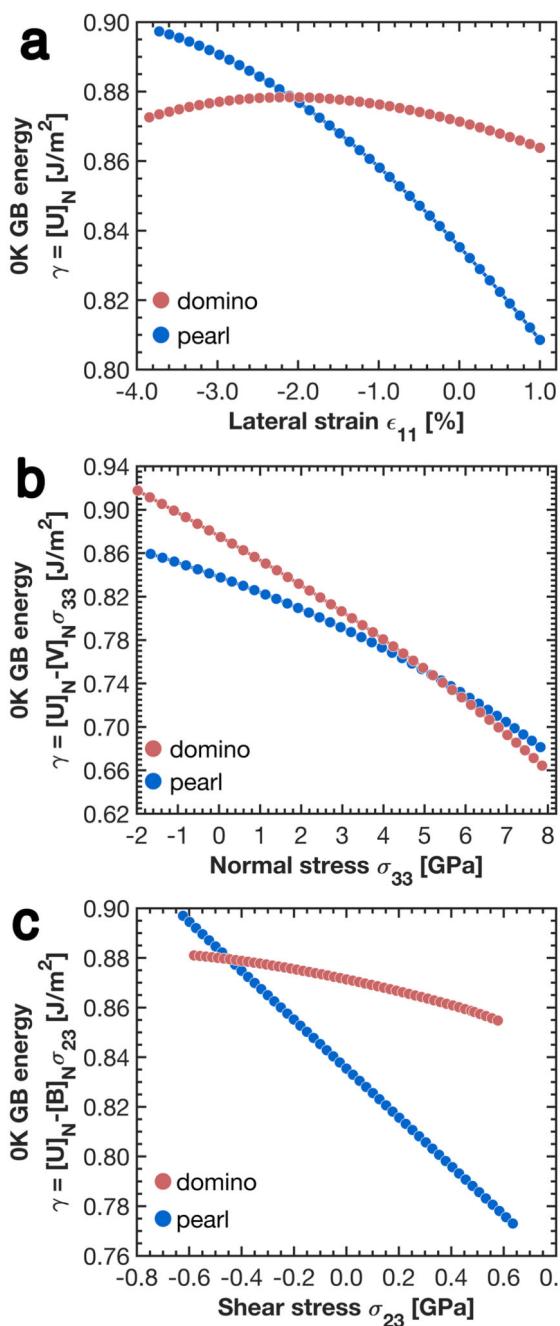
a. Nucleation of a pearl GB phase at the open surface (left) of the asymmetric GB at 600K.

b. Asymmetric pearl GB phase after the transformation at 600K is complete. The boundary remains asymmetric.



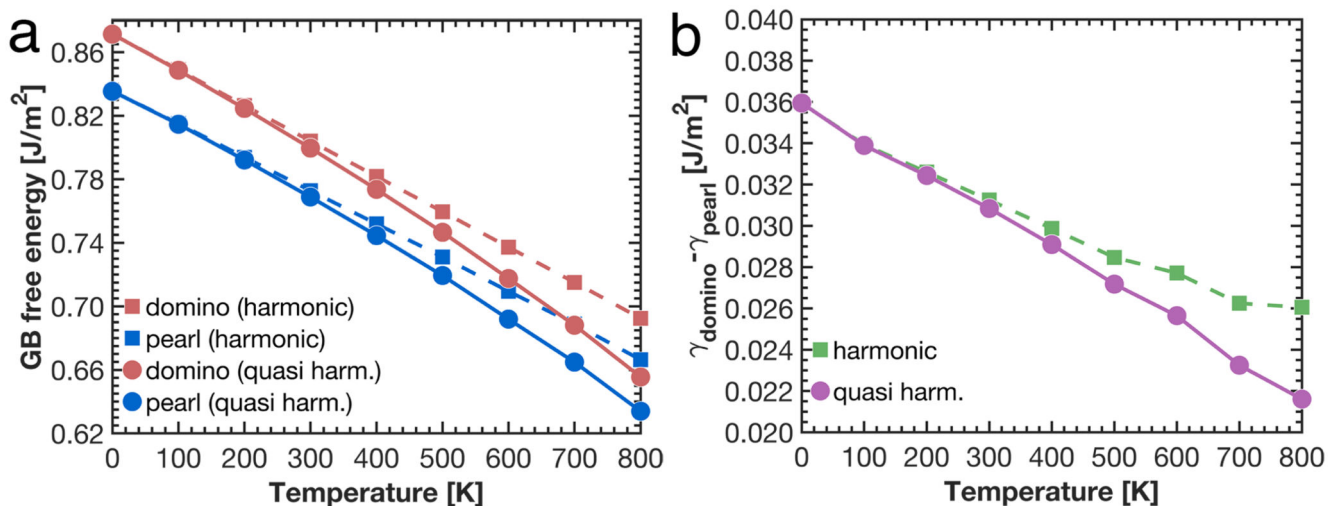
Extended Data Fig. 6. Asymmetric grain boundary transformation at 700K.

a and **b** show the nucleation of the pearl GB phase from the open surface on the left of the simulation cell annealed at 700K. **c** and **d** from the right. **e**, The initially asymmetric domino structure transformed into a symmetric pearl phase in MD at 700K after the transformation is complete.



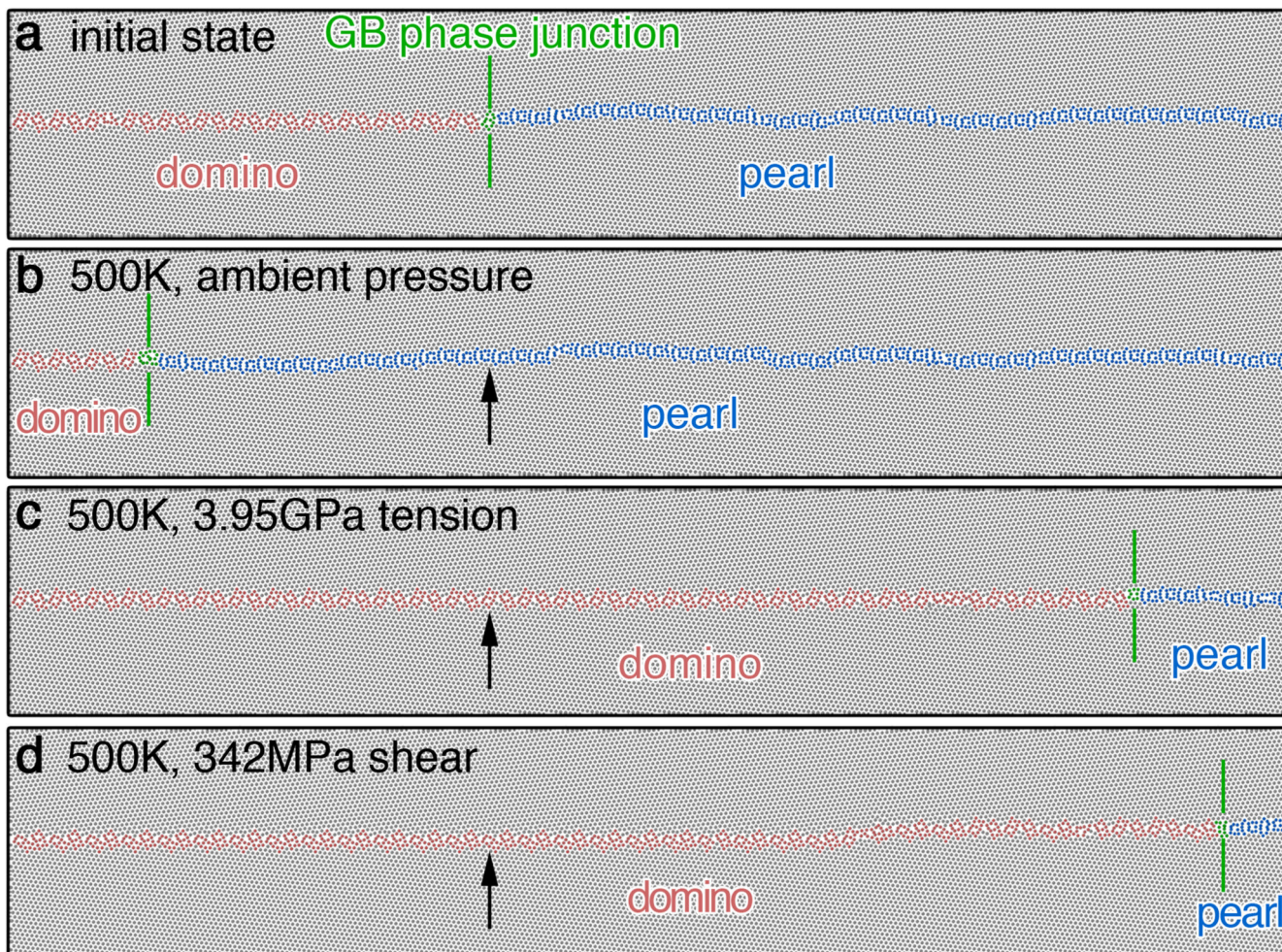
Extended Data Fig. 7. Stress-dependent GB excess enthalpies.

OK calculations of GB excess enthalpies γ_{domino} and γ_{pearl} to estimate stresses and strains required to stabilize domino phase and achieve equilibrium coexistence in the model. GB excess energy curves cross at **a**, lateral strain $\epsilon_{11}^* = 2\%$, **b**, tensile stress $\sigma_{33}^* = 5$ GPa and **c**, shear stress parallel the GB along the tilt axis $\sigma_{23}^* = 440$ MPa. Here, $[U]_N$, $[V]_N$ and $[B]_N$ are excess GB energy, volume and shear, respectively.



Extended Data Fig. 8. Grain boundary free energies.

a. GB free energies of domino and pearl phases as functions of temperature at zero bulk stress calculated using harmonic and quasi-harmonic approximations. **b.** GB free energy difference $\gamma_{domino} - \gamma_{pearl}$ as a function of temperature decreases but remains positive suggesting that at ambient pressure domino phase remains metastable in our model. These calculations are consistent with domino to pearl transformations simulated directly with MD. They also show that in the model the relative stability of domino improves with temperature since the GB free energy difference decreases by about 30% relative to 0K.



Extended Data Fig. 9. Finite temperature GB phase transformations under stress.

MD simulations of GB phase transformations and equilibrium coexistence at 500K under **a**, **b** ambient conditions **c** tensile stress and **d** shear stress. To avoid hysteresis due to nucleation barrier we start with a two phase state shown in **a** and monitor the direction of the GB phase junction migration. **b**, At ambient conditions pearl phase grows and the junctions moves to the left. **c**, Under tensile stress of 3.95 GPa domino becomes thermodynamically more stable, it grows at the expense of pearl and the junction moves to the right. **d**, Under shear stress of 342 MPa parallel to the GB plane in the direction parallel to the tilt axis domino phase also becomes more stable and grows. The back arrow indicates the initial position of the GB phase junction, while the green line shows the final position. We performed similar simulations at different tensile and shear stresses and conclude that in the model the equilibrium coexistence between pearl and domino phases at this temperature of 500K can be achieved around 3.3 GPa tension or 200-350 MPa interval of shear stress. The simulations of equilibrium coexistence confirm that pearl and domino are examples of GB phases. The MD simulations ran for 200 to 400 ns.

Extended Data Tab. 1
Excess thermodynamic properties.

Table showing the energy, excess volume, excess stress and number of inserted atoms [*n*] of the ground state pearl and the lowest energy domino GB phases determined at 0K.

GB phase	Energy [J/m ²]	Volume [Å]	Stress τ_{11} [J/m ²]	Stress τ_{22} [J/m ²]	[<i>n</i>]
Pearl	0.835	0.14	-1.66	-0.46	0
Domino	0.871	0.22	0.25	0.29	0

Supplementary Material

Refer to Web version on PubMed Central for supplementary material.

Acknowledgments

The authors thank Dr. Gunther Richter and his team from the Max-Planck-Institute for Intelligent Systems for producing the Cu thin films by molecular beam epitaxy. TF is grateful to R. Freitas for the help with the free energy calculations. GD and TM acknowledges financial support from the European Research Council (ERC) through Grant No. 787446 — GB-CORRELATE. Support for TF and RER was provided under the auspices of the U.S. Department of Energy by Lawrence Livermore National Laboratory under Contract DE-AC52-07NA27344. TF and RER were funded by the Laboratory Directed Research and Development Program at LLNL under Project Tracking Code No. 19-ERD-026.

References

- Sutton, AP, Balluffi, RW. Interfaces in crystalline materials. Clarendon Press; Oxford: 1995.
- Hart EW. Two-dimensional phase transformation in grain boundaries. *Scr Metall.* 1968; 2:179–182.
- Hart, EW. Chap. Grain Boundary Phase Transformations The Nature and Behavior of Grain Boundaries. Springer; US: 1972. 155–170.
- Cahn JW. Transitions and Phase Equilibria Among Grain Boundary Structures. *J Phys Colloq.* 1982; 43:199–213.
- Rottman C. Theory of Phase Transitions at Internal Interfaces. *J Phys Colloq.* 1988; 49:313–326.
- Han J, Vitek V, Srolovitz DJ. Grain-boundary metastability and its statistical properties. *Acta Mater.* 2016; 104:259–273.
- Tang M, Carter WC, Cannon RM. Diffuse interface model for structural transitions of grain boundaries. *Phys Rev B.* 2006; 73
- Dillon SJ, Tang M, Carter WC, Harmer MP. Complexion: A new concept for kinetic engineering in materials science. *Acta Mater.* 2007; 55:6208–6218.
- Luo J, Cheng H, Asl KM, Kiely CJ, Harmer MP. The Role of a Bilayer Interfacial Phase on Liquid Metal Embrittlement. *Science.* 2011; 333:1730–1733. [PubMed: 21940889]
- Cantwell PR, et al. Grain boundary complexions. *Acta Mater.* 2014; 62:1–48.
- Udler D, Seidman DN. Congruent phase transition at a twist boundary induced by solute segregation. *Phys Rev Lett.* 1996; 77:3379–3382. [PubMed: 10062205]
- Duscher G, Chisholm MF, Alber U, Rühle M. Bismuth-induced embrittlement of copper grain boundaries. *Nat Mater.* 2004; 3:621–626. [PubMed: 15322533]
- Schweinfest R, Paxton AT, Finnis Michael W. Bismuth embrittlement of copper is an atomic size effect. *Nature.* 2004; 432:1008–1011. [PubMed: 15616557]
- Tang M, Carter WC, Cannon RM. Grain boundary transitions in binary alloys. *Phys Rev Lett.* 2006; 97

15. Dillon SJ, Harmer MP, Luo J. Grain boundary complexions in ceramics and metals: An overview. *JOM*. 2009; 61:38–44.
16. Wang Z, et al. Atom-resolved imaging of ordered defect superstructures at individual grain boundaries. *Nature*. 2011; 479:380–383. [PubMed: 22094698]
17. Rohrer GS. The role of grain boundary energy in grain boundary complexion transitions. *Curr Opin Solid St M*. 2016; 20:231–239.
18. Zhou N, Hu T, Luo J. Grain boundary complexions in multicomponent alloys: Challenges and opportunities. *Curr Opin Solid St M*. 2016; 20:268–277.
19. Yu Z, et al. Segregation-induced ordered superstructures at general grain boundaries in a nickel-bismuth alloy. *Science*. 2017; 358:97–101. [PubMed: 28983049]
20. Frolov T, Olmsted DL, Asta M, Mishin Y. Structural phase transformations in metallic grain boundaries. *Nat Commun*. 2013; 4:1899. [PubMed: 23695693]
21. Zhu Q, Samanta A, Li B, Rudd RE, Frolov T. Predicting phase behavior of grain boundaries with evolutionary search and machine learning. *Nat Commun*. 2018; 9:467. [PubMed: 29391453]
22. Carrion F, Kalonji G, Yip S. Evidence for grain boundary phase transition in a 2D bicrystal. *Scr Metall*. 1983; 17:915–918.
23. Frolov T, Rudd RE, Zhu Q, Marian J. Grain boundary phases in bcc metals. *Nanoscale*. 2018; 10:8253–8268. [PubMed: 29687111]
24. Chua AL, Benedek NA, Chen L, Finnis MW, Sutton AP. A genetic algorithm for predicting the structures of interfaces in multi-component systems. *Nat Mater*. 2010; 9:418–422. [PubMed: 20190770]
25. Oganov AR, Glass CW. Crystal structure prediction using ab initio evolutionary techniques: Principles and applications. *J Chem Phys*. 2006; 124
26. Lyakhov AO, Oganov AR, Stokes HT, Zhu Q. New developments in evolutionary structure prediction algorithm USPEX. *Comput Phys Commun*. 2013; 184:1172–1182.
27. Maksimova EL, Shvindlerman LS, Straumal BB. Transformation of Σ 17 special tilt boundaries to general boundaries in tin. *Acta Metall*. 1988; 36:1573–1583.
28. Rabkin E, Minkwitz C, Herzig CH, Klinger L. Evidence for structural multiplicity of the $\Sigma = 3$ incoherent twin boundary in cu from grain-boundary diffusion measurements. *Phil Mag Lett*. 1999; 79:409–415.
29. Divinski SV, Edelhoff H, Prokofjev S. Diffusion and segregation of silver in copper Σ 5(310) grain boundary. *Phys Rev B*. 2012; 85
30. Dehm G, Edongué H, Wagner T, Oh SH, Arzt E. Obtaining different orientation relationships for Cu films grown on (0001) α -Al₂O₃ substrates by magnetron sputtering. *Zeitschrift fuer Metallkunde / Materials Research and Advanced Techniques*. 2005; 96:249–254.
31. Freitas R, Asta M, de Koning M. Nonequilibrium free-energy calculation of solids using LAMMPS. *Comput Mater Sci*. 2016; 112:333.
32. Freitas R, Rudd RE, Asta M, Frolov T. Free energy of grain boundary phases: Atomistic calculations for Σ 5(310)[001] grain boundary in Cu. *Phys Rev Mater*. 2018; 2
33. Aramfard M, Deng C. Mechanically enhanced grain boundary structural phase transformation in Cu. *Acta Mater*. 2018; 146:304–313.
34. Khalajhedayati A, Pan Z, Rupert TJ. Manipulating the interfacial structure of nanomaterials to achieve a unique combination of strength and ductility. *Nat Commun*. 2016; 7
35. Phillips MA, et al. X-ray microdiffraction: Local stress distributions in polycrystalline and epitaxial thin films. *Microelec Eng*. 2004; 75:117–126.
36. Dehm G, Balk TJ, Edongué H, Arzt E. Small-scale plasticity in thin Cu and Al films. *Microelec Eng*. 2003; 70:412–424.
37. Pryor A, Ophus C, Miao J. A Streaming Multi-GPU Implementation of Image Simulation Algorithms for Scanning Transmission Electron Microscopy. *Adv Struct Chem Imag*. 2017; 3:15.
38. Ophus C. A Fast Image Simulation Algorithm for Scanning Transmission Electron Microscopy. *Adv Struct Chem Imag*. 2017; 3:13.
39. Plimpton S. Fast parallel algorithms for short-range molecular dynamics. *J Comput Phys*. 1995; 117:1–19.

40. Stukowski A. Visualization and analysis of atomistic simulation data with OVITO-the Open Visualization Tool. *Modelling Simul Mater Sci Eng.* 2010; 18
41. Peter NJ, et al. Segregation-Induced Nanofaceting Transition at an Asymmetric Tilt Grain Boundary in Copper. *Phys Rev Let.* 2018; 121
42. Foiles SM. Evaluation of harmonic methods for calculating the free energy of defects in solids. *Phys Rev B.* 1994; 49:14930–14938.
43. Gibbs, JW. *The Collected Work of J. William Gibbs. Vol. 1.* Longmans, Green and Co.; 1928.
44. Frolov T, Mishin Y. Thermodynamics of coherent interfaces under mechanical stresses. I. Theory. *Phys Rev B.* 2012; 85
45. Frolov T, Mishin Y. Thermodynamics of coherent interfaces under mechanical stresses. II. Application to atomistic simulation of grain boundaries. *Phys Rev B.* 2012; 85

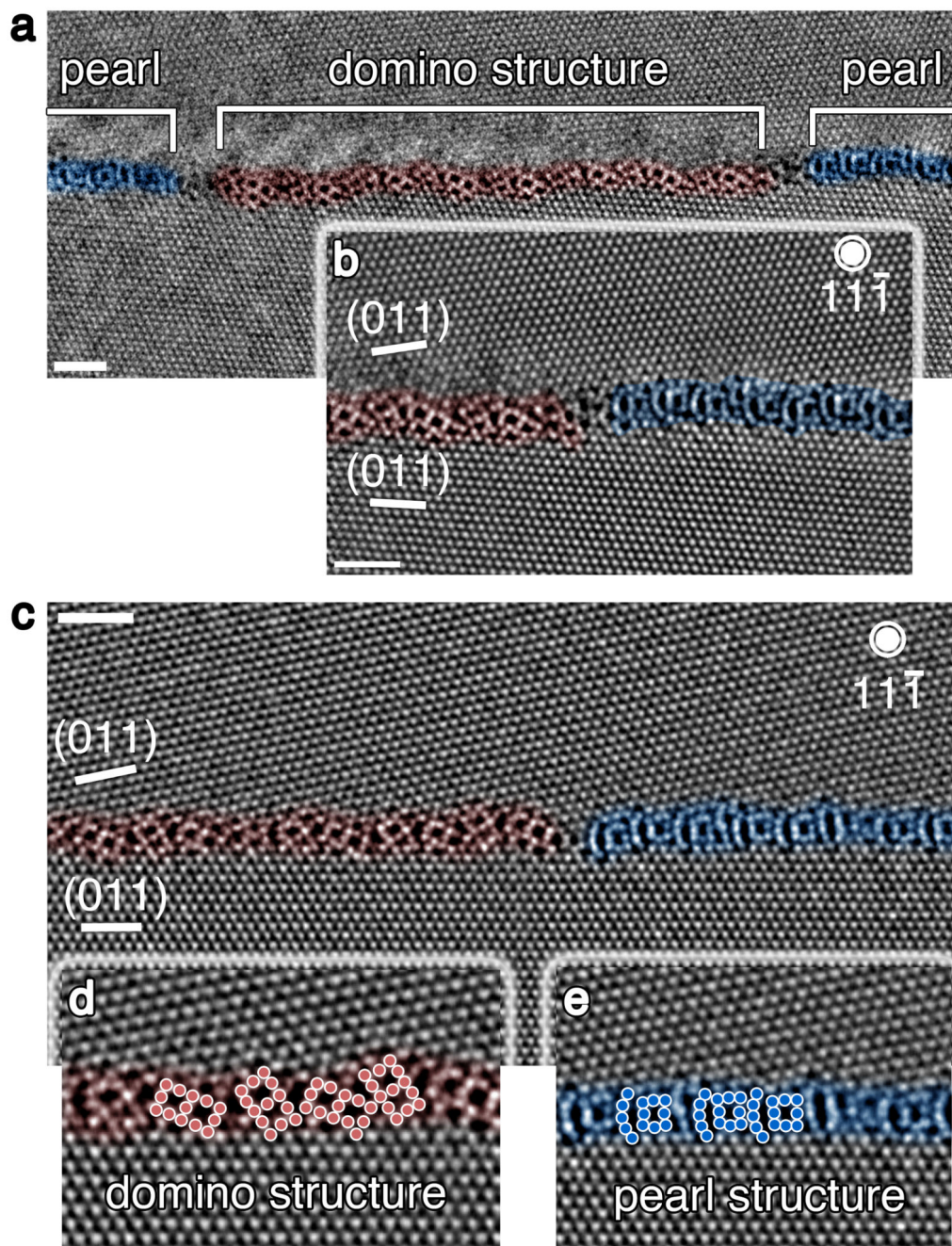


Fig. 1. HAADF-STEM images of two congruent GB phase transitions.

a. Overview image of the transition at a near symmetric Σ 19b [11-1] GB with (178) boundary plane. The domino and pearl structures (or GB phases) are highlighted in red and blue, respectively. The overall misorientation of the GB is $\sim 48^\circ$ with a deviation in inclination from the symmetric orientation of $\sim 1^\circ$. **b.** Magnified view of the GB transition on the right highlighting the differences in structural units of both boundary segments. **c.** GB phase transition at a vicinal Σ 19b [11-1] GB with $\sim 47^\circ$ misorientation and boundary planes of (011) lower grain and (279) upper grain. **(d)** and **(e)** illustrate close-up images of the

domino and pearl structure of the vicinal boundary, respectively. The scale bar is 1 nm in all images.

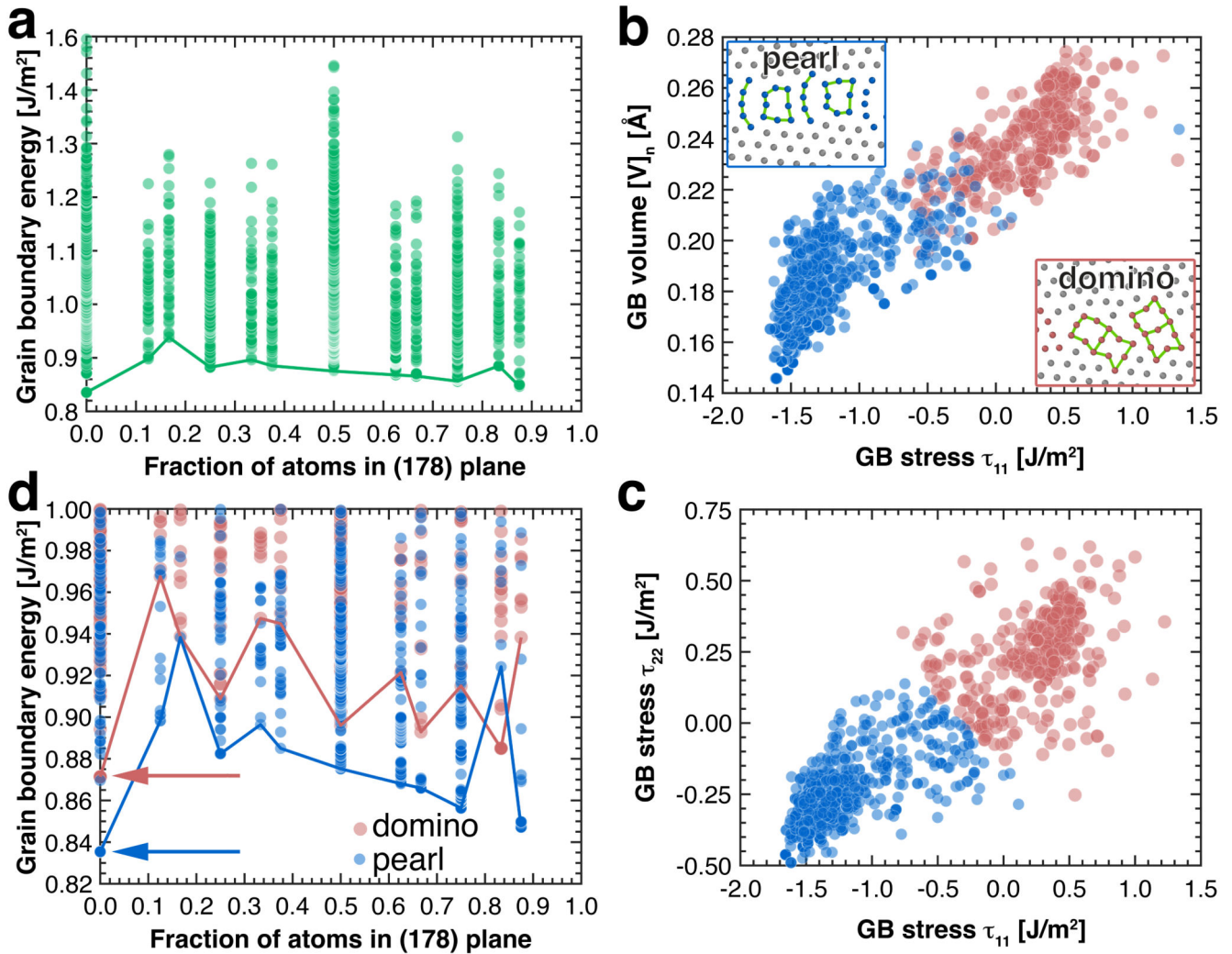


Fig. 2. Evolutionary GB structure search and clustering analysis predicts pearl and domino GB phases of the $\Sigma 19b$ (178) [11-1] GBs.

a. Grain boundary energy of the generated structures plotted versus the number of inserted atoms calculated as a fraction of the (178) bulk plane. The solid line connects the lowest energy structures with different numbers of atoms. **b.** Excess volume of the generated structures plotted versus excess grain boundary stress τ_{11} . **c.** Excess GB stress τ_{22} of the generated structures plotted versus excess grain boundary stress τ_{11} . The two clusters in the space of GB properties [V_n , τ_{11} and τ_{22}] were automatically identified using the K-means clustering algorithm. The two clusters colored in blue and red correspond to pearl and domino phases, respectively. The lowest energy structures of domino and pearl are given as insets in **b**. **d.** GB energy versus the number of atoms, same as in **a** with points assigned to pearl or domino. The arrows indicate the ground state structures of pearl and domino, respectively. The lowest energy configurations have the same number of atoms.

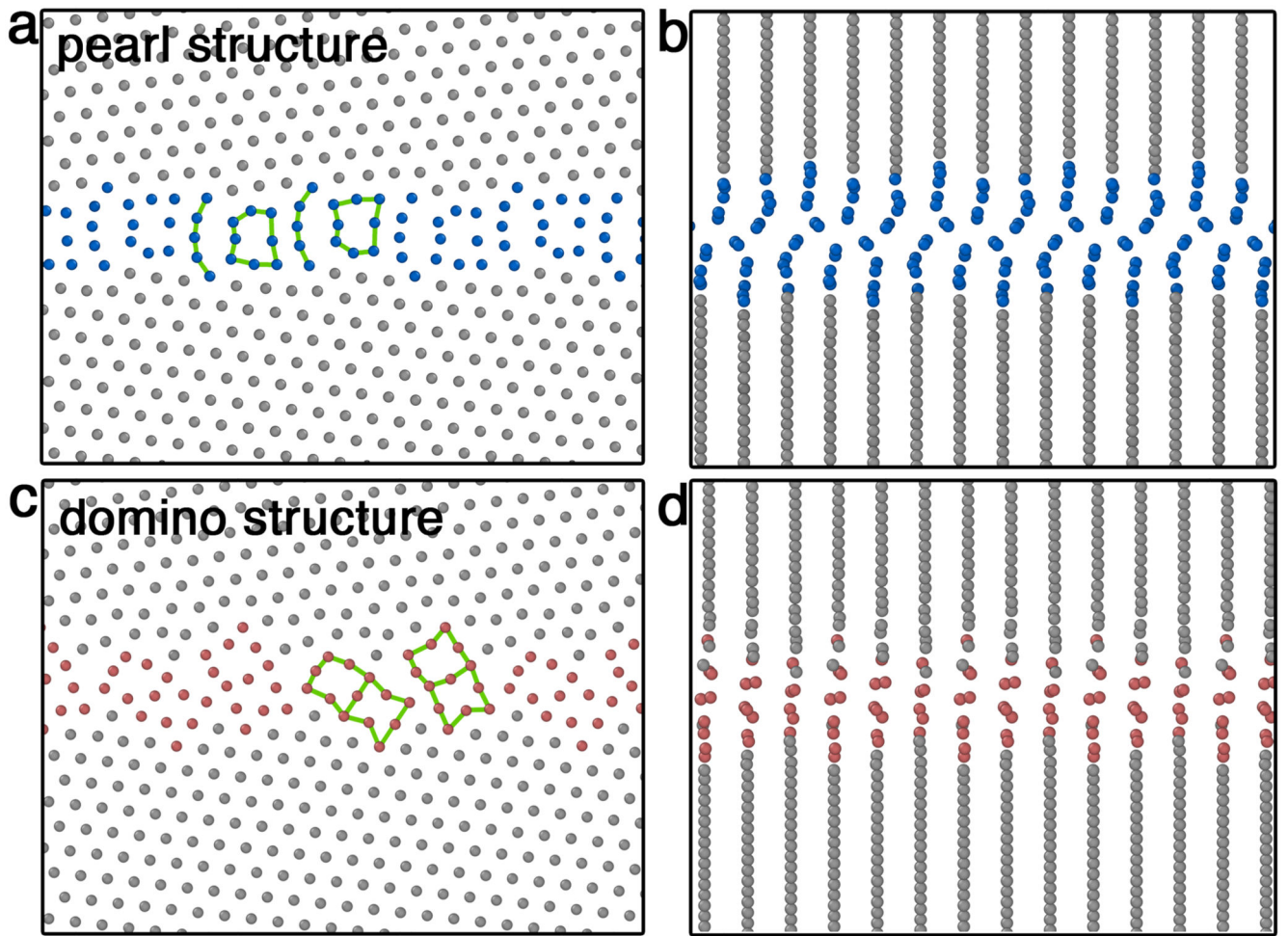


Fig. 3. Structures of the pearl and domino GB phases predicted by the evolutionary search. **a** and **c** show projections along the $[11-1]$ tilt axis of the pearl and domino phases, respectively. **b** and **d** visualize the GB structures perpendicular to the tilt axis viewed along $[5-32]$.

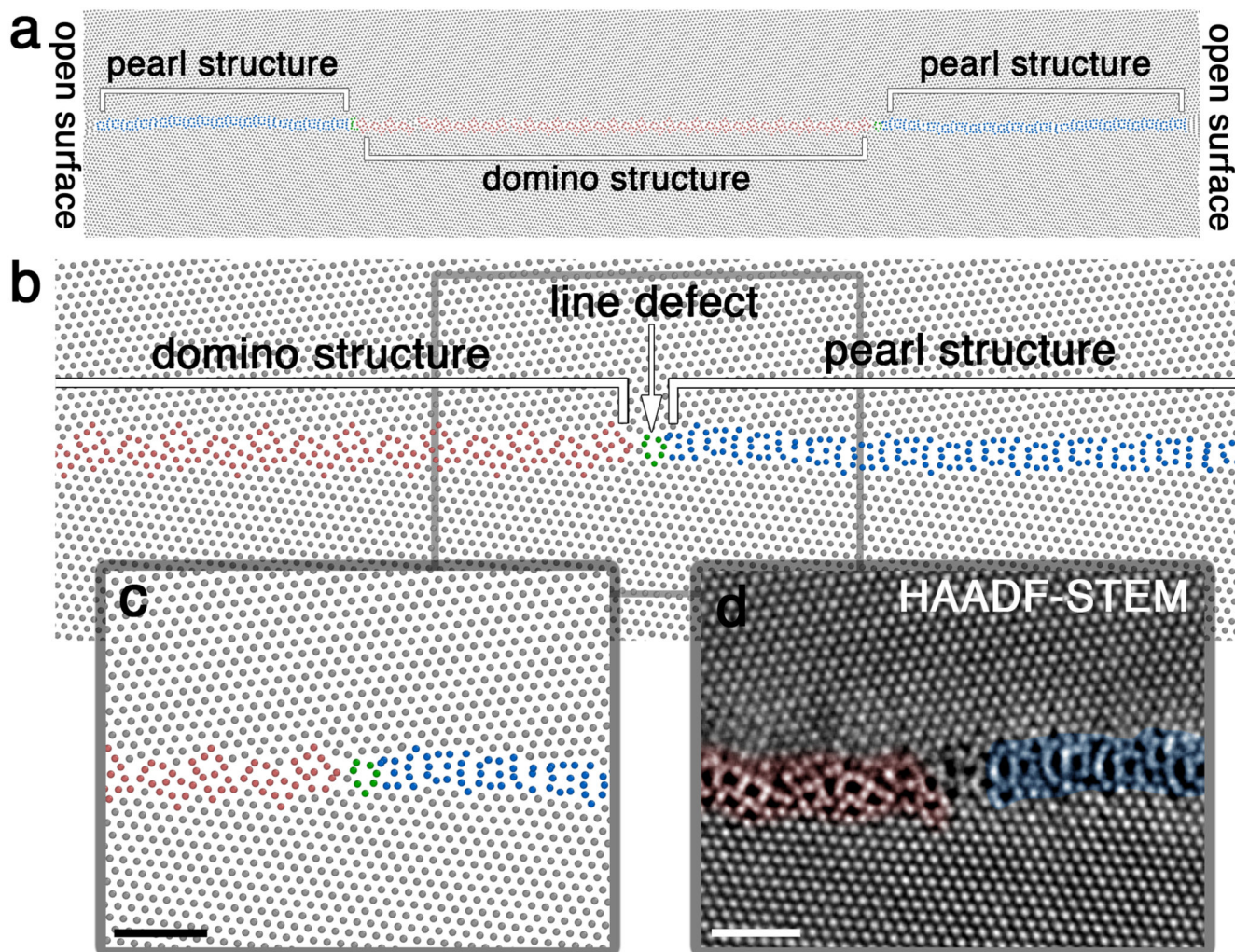


Fig. 4. Simulated grain boundary phase transition at finite temperature.

a, MD simulation cell with open surfaces of a $\Sigma 19b$ (178) [11-1] tilt GB viewed along the tilt axis. The domino phase is highlighted in red, the pearl phase in blue. **b**, Close up of the right-side phase transition with indication of the grain boundary phase junction (line defect, green), separating the two GB phases. **c**, Magnified view of the line defect and phase coexistence of domino and pearl phase. **d**, Experimental HAADF-STEM image of the symmetric GB phase transition shown in Fig. 1b. The scale bar is 1 nm.